High Thermoelectric Performance in Crystallographically Textured *n*-type $Bi_2Te_{3-x}Se_x$ Produced from Asymmetric Colloidal Nanocrystals

Yu Liu,[†] Yu Zhang,[†] Khak Ho Lim,[‡] Maria Ibáñez,[§,⊥] Silvia Ortega,[†] Mengyao Li,[†] Jérémy David,[¶] Sara Martí-Sánchez,[¶] Ka Ming Ng,[‡] Jordi Arbiol,[¶,//] Maksym V. Kovalenko,[§,⊥] Doris Cadavid,[,†,○] Andreu Cabot*[,†,//]*

[†] Catalonia Energy Research Institute - IREC, Sant Adria de Besòs, 08930 Barcelona, Spain.

[‡] Department of Chemical and Biological Engineering, Hong Kong University of Science and Technology, Hong Kong, China.

[§] Institute of Inorganic Chemistry, Department of Chemistry and Applied Biosciences, ETH Zürich, Vladimir Prelog Weg 1, CH-8093, Switzerland.

[⊥] Empa—Swiss Federal Laboratories for Materials Science and Technology, Dübendorf, Überlandstrasse 129, CH-8600, Switzerland.

[¶] Catalan Institute of Nanoscience and Nanotechnology (ICN2), CSIC and BIST, Campus UAB, Bellaterra, 08193 Barcelona, Catalonia, Spain.

[//] ICREA, Pg. Lluis Companys 23, 08010 Barcelona, Spain.

[○] Departamento de Física, Universidad Nacional de Colombia, 111321, Ciudad Universitaria, Bogotá, Colombia.

* Email: acabot@irec.cat

* Email: dycadavidr@unal.edu.co

ABSTRACT

In the present work, we demonstrate crystallographically textured *n*-type $Bi_2Te_{3-x}Se_x$ nanomaterials with exceptional thermoelectric (TE) figures of merit produced by consolidating disk-shaped $Bi_2Te_{3-x}Se_x$ colloidal nanocrystals (NCs). Crystallographic texture was achieved by hot pressing the asymmetric NCs in the presence of an excess of tellurium. During the hot press, tellurium acted both as lubricant to facilitate the rotation of NCs lying close to normal to the pressure axis and as solvent to dissolve the NCs approximately aligned with the pressing direction, which afterward recrystallize with a preferential orientation. NC-based $Bi_2Te_{3-x}Se_x$ nanomaterials showed very high electrical conductivities associated to large charge carrier concentrations, *n*. We hypothesize that such large *n* resulted from the presence of an excess of tellurium during processing, which introduced a high density of donor Ti_{Bi} antisites. Additionally, the presence in between grains of traces of elemental Te, a narrow band gap semiconductor with a work function well below $Bi_2Te_{3-x}Se_x$, might further contribute to increase *n* through spillover of electrons, while at the same time blocking phonon propagation and hole transport through the nanomaterial. NC-based $Bi_2Te_{3-x}Se_x$ nanomaterials were characterized by very low thermal conductivities in the pressing direction, which resulted in *ZT* values up to 1.31 at 438 K in this direction. This corresponds to a *ca.* 40 % ZT enhancement from commercial ingots. Additionally, high *ZT* values were extended over wider temperature ranges due to reduced bipolar contribution to the Seebeck coefficient and the thermal conductivity. Average *ZT* values up to 1.15 over a wide temperature range, 320 K to 500 K, were measured, which corresponds to a *ca.* 50 % increase over commercial materials in the same temperature range. Contrary to most previous works, highest *ZT* values were obtained in the pressing direction, corresponding to the *c* crystallographic axis, due to the predominance of the thermal conductivity reduction over the electrical conductivity difference when comparing the two crystal directions.

KEYWORDS: $Bi_2Te_{3-x}Se_x$, nanocrystal, colloid, crystallographic texture, liquid phase sintering, thermoelectricity.

The recovery of the huge amounts of energy wasted in the form of heat in transportation and in all industrial and domestic processes is an extremely appealing pursuit both from economic and environmental points of view.[1, 2] This goal requires the use of a distributed network of modular and cost-effective systems that convert heat into electricity. With the steam turbines being not suitable for small scale and portable generation, solid state thermoelectric (TE) devices become a worthwhile alternative. TE devices contain *n*-type and *p*-type semiconductors connected thermally in parallel and electrically in series. They can be manufactured with virtually any size, are highly durable and can be adapted to harvest energy from any temperature gradient.[1, 3] However, their widespread implementation requires improving their cost-effectiveness by increasing energy conversion efficiency and/or reducing manufacturing costs.

The energy conversion efficiency of a TE device can be analytically expressed in terms of the temperature at the hot and cold sides and a unique material-dependent figure of merit (Z), which is generally expressed in an dimensionless form: $ZT = \sigma S^2 T/\kappa$, where T is the absolute temperature, σ the electrical conductivity, S the Seebeck coefficient and κ the thermal conductivity.[2, 4-6] Nanostructured materials have been proven successful in meeting the very demanding set of interrelated properties that maximize the TE figure of merit, *i.e.* high σ and S, and low κ.[4, 7-10] An additional advantage of nanomaterials is their superior mechanical robustness as compared to fragile single crystals.[11, 12]

While numerous approaches to produce nanomaterials exist, nanocrystal (NC)-based bottom-up strategies allow an unparalleled combination of delicate control over material parameters with high production throughputs.[5, 13-17] In this regard, NC-based approaches offer clear advantages over currently more conventional nanomaterial fabrication methods, which lack sufficient control over material parameters, *e.g.* ball milling,[18] and/or are too costly for an eventual large volume industrial manufacturing of cost-effective TE modules, *e.g.* vacuum-based thin film technologies.[19]

Bi_2Te_3-based alloys are the most widely used TE materials for operation at ambient temperatures, being commercialized for refrigeration and used in radioisotope TE generation systems since several decades ago.[8, 20] In recent years, great progress has been made in improving the figure of merit of the *p*-type Bi_2Te_3-based alloy,[3, 18, 21-25] reaching record ZT values up to 1.96 at 420 K and of 1.77 when averaged over a wide temperature range 320 – 500 K.[24] On the other hand, the performance of *n*-type Bi_2Te_3-based materials, $Bi_2Te_{3-x}Se_x$, lags substantially behind, with ZT values just above 1.[26-34]

Structurally, Bi_2Te_3 crystallizes in a rhombohedral crystal phase ($R\bar{3}m$ space group, Table S1) and can be viewed as a layered material consisting of stacked quintuple layers Te-Bi-Te-Bi-Te along the *c*-axis bonded together by weak van der Waals interactions (Figure S1).[35] Such layered structure results in highly anisotropic transport properties. In particular, *n*-type $Bi_2Te_{2.6}Se_{0.4}$ single crystals are characterized by electrical and thermal conductivities in the *ab* plane that are ~4.38 times and over 2 times higher than along the *c* axis, respectively.[36]

The strong anisotropy of its transport properties requires producing $Bi_2Te_{3-x}Se_x$ nanomaterials with proper crystallographic texture. Such textured $Bi_2Te_{3-x}Se_x$ samples have been produced using a variety of strategies,[28, 37-41] but without significantly increasing the material figure of merit over un-textured samples, probably due to a lack of the simultaneous optimization of the microstructure, composition and point defects.

In the present work, we demonstrate that using asymmetric colloidal $Bi_2Te_{3-x}Se_x$ NCs with controlled composition (x = 0, 0.2, 0.3, 0.4, 0.5 and 0.7) and a proper consolidation process, highly textured nanomaterials with high relative densities and outstanding TE figures of merit can be produced.

RESULTS AND DISCUSSION

$Bi_2Te_{3-x}Se_x$ NCs

$Bi_2Te_{3-x}Se_x$ NCs with variable composition (x = 0, 0.2, 0.3, 0.4, 0.5 and 0.7) were produced through a modified polyol method, using ethylene glycol (EG) as a high boiling point solvent and reducing agent (see experimental part for details).[23, 31-33, 42-44] Conveniently, the $Bi_2Te_{3-x}Se_x$ NC composition (x) could be tuned by adjusting the initial ratios of Se and Te precursors (Table 1). This synthetic protocol, including the purification step, was characterized by material yields above 95 % and it was optimized to produce *ca.* 4 g of NCs per batch. Figures 1a and S2 show representative SEM micrograph of the disk-shaped $Bi_2Te_{3-x}Se_x$ NCs obtained following this procedure. As measured from SEM images, NCs had average lateral dimensions of 480 ± 100 nm and an average thickness of 35 ± 8 nm (Figure S3). Within the tested range, no effect of the Se concentration on the NC size was observed.

Excess amounts of Te, nominally 25 mol%, were introduced in the reaction mixture. This Te excess was found in the form of thin Te nanorods segregated from $Bi_2Te_{3-x}Se_x$ nanodisks (Figures 1 and S2). The segregation of the Te excess was very convenient for the present work, but at the same time somehow surprising. Notice that the reaction of the Te precursor in the exact same conditions as those used to produce $Bi_2Te_{3-x}Se_x$ NCs, but in the absence of the Bi and Se precursors, resulted in the formation of Te nanorods (Figure S4). Even lower reaction temperatures than those necessary to produce $Bi_2Te_{3-x}Se_x$ NCs sufficed to reduce the Te precursor and form the Te nanorods. On the other hand, the reaction of the Se precursor alone did not result in the formation of Se particles (Figure S5). The reaction of a mixture of Se and Te precursors resulted again in Te nanorods, with no Te-Se compound (Figure S6). We hypothesize that the formation of $Bi_2Te_{3-x}Se_x$ NCs proceeded through the initial nucleation of Te NCs and the posterior incorporation of Bi and Se atoms within the structure, with the concomitant geometric and crystallographic evolution from the initial Te nanorods to the final $Bi_2Te_{3-x}Se_x$ nanodisks. Because the differential energy of Se within the $Bi_2Te_{3-x}Se_x$ lattice and in solution is higher than that of Te, $Bi_2Te_{3-x}Se_x$ NCs with the Bi:Se ration of the precursor mixture were obtained and the excess of Te was found in the form of segregated elemental particles (Figure S7).

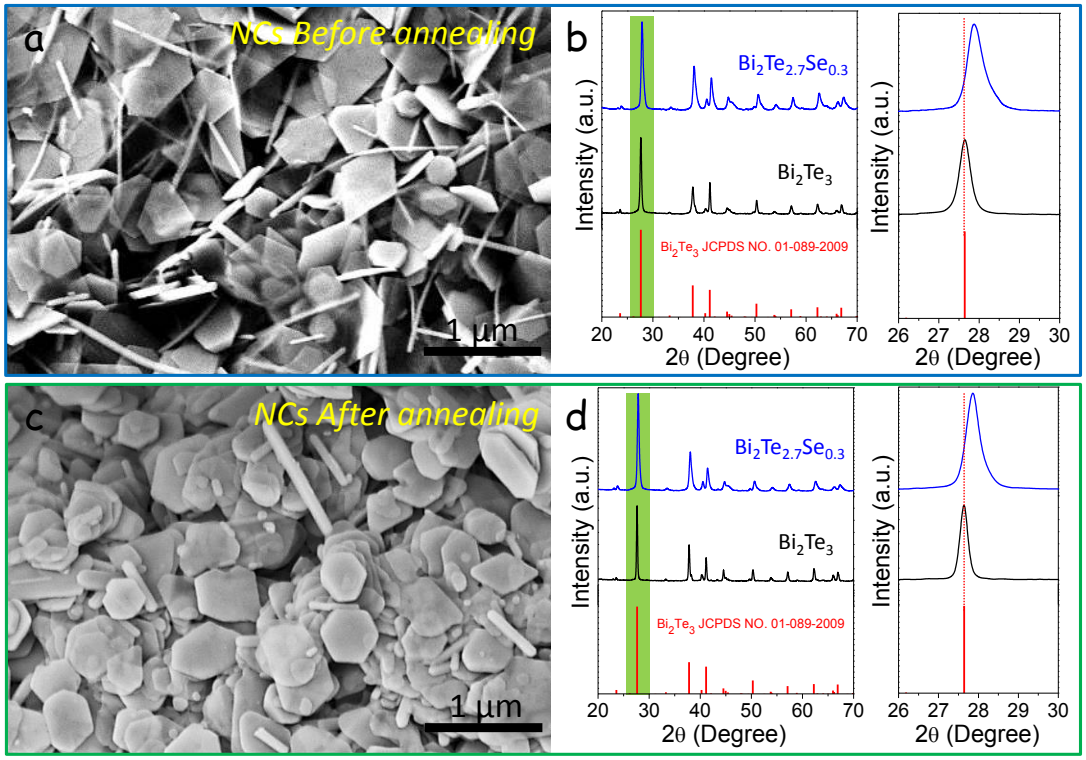

Figure 1. Representative SEM images (a, c) and XRD patterns (b, d) of the $Bi_2Te_{3-x}Se_x$ disk-shaped NCs produced and used in this work, before (a, b) and after (c, d) annealing at 350°C for 60 min. A detail of the same XRD pattern showing the shift of the (015) peak with the Se composition (x=0, 0.3) is also provided. The standard Bi_2Te_3 diffraction pattern (JCPDS NO. 01-089-2009) is included as reference.

$Bi_2Te_{3-x}Se_x$ NCs were purified by multiple precipitation and redispersion steps using several solvents to remove the different impurities, as detailed in the experimental section. Subsequently, they were dried and, to remove any remaining trace of surfactant, they were annealed at 350 °C for 60 min under argon flow inside a tube furnace (Figure S8). The annealed $Bi_2Te_{3-x}Se_x$ NCs conserved the original disk shape (Figure S9), but during annealing their edges became smoother and the lateral size and thickness slightly increased. The size of the Te nanorods particularly increased as observed in Figures 1c and S9.

SEM-EDX analysis showed the NC composition, particularly the Bi:Se ratios, to precisely follow the nominal values (Table 1 and Figure S10), both before and after the annealing treatment. The excess of Te was measured at around 20 mol% instead of the nominal 25 mol% both before and after annealing. Within the EDX experimental error, $Bi_2Te_{3-x}Se_x$ NCs produced without an excess of Te showed similar compositions.

Table 1. SEM-EDX composition (related to Bi = 2) of $Bi_2Te_{3-x}Se_x$ NCs (x = 0, 0.2, 0.3, 0.4, 0.5 and 0.7), and respective annealed NCs and consolidated pellets. Data was obtained from averaging 5 analyses, resulting in an estimated error of *ca.* 3 %. An additional Te excess of 25 mol% was introduced in all the samples.

Nominal x / Material	x = 0		x = 0.2		x = 0.3		x = 0.4		x = 0.5		x = 0.7	
	Te	Se	Te	Se	Te	Se	Te	Se	Te	Se	Te	Se
NCs	3.60	0.0	3.19	0.19	3.12	0.29	3.09	0.40	3.01	0.50	2.90	0.71
Annealed NCs	3.58	0.0	3.20	0.20	3.11	0.29	3.08	0.39	3.00	0.51	2.89	0.72
Pellet	3.04	0.0	2.79	0.20	2.73	0.30	2.61	0.39	2.48	0.46	2.30	0.73

XRD analyses of the initial NCs and the annealed NCs showed no secondary phases (Figures 1b, 1d and S11), not even elemental Te due to its relatively low amount. XRD peaks linearly shifted with the Se concentration to higher diffraction angles, as it corresponds to a lattice contraction due to the substitution of Te by Se atoms (Figure S12). The following of a Vegard's law evidenced the presence of increasing amounts of Se within the alloy crystal lattice.

Consolidation of $Bi_2Te_{3-x}Se_x$ NCs

Annealed $Bi_2Te_{3-x}Se_x$ NCs were hot-pressed within an inert atmosphere into cylindrical pellets (see experimental section for details). As measured by the Archimedes' method, the relative densities of the produced materials were *ca.* 93 %, as calculated from a linear regression with the Se content of the theoretical values for Bi_2Te_3 and Bi_2Se_3 (Table S2).

XRD analysis of the cylindrical pellets hold in two perpendicular directions, with the cylinder plane normal and parallel to the diffraction plane, demonstrated the consolidated material to be characterized with a significant crystallographic texture, with the [001] crystallographic direction oriented along the press axis (Figure 2).

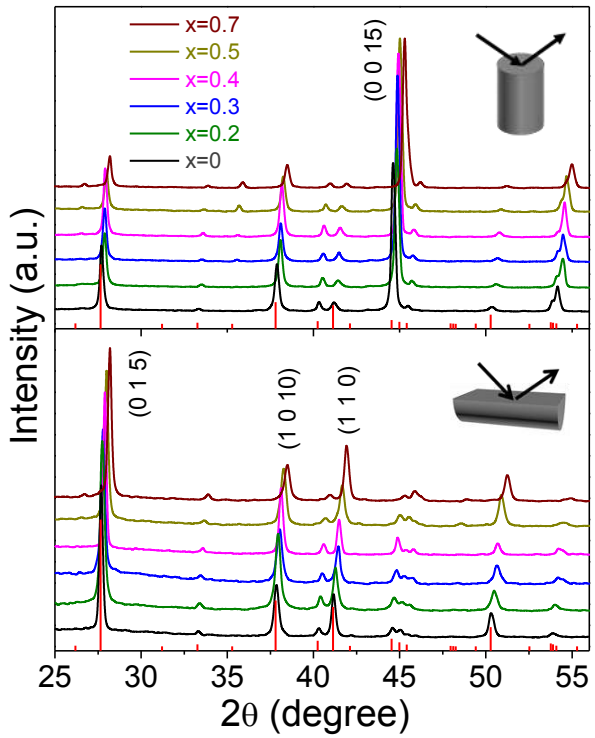

Figure 2. XRD patterns of consolidated $Bi_2Te_{3-x}Se_x$ pellets measured in the two directions, parallel and normal to the pressing direction.

Cross-section SEM micrographs showed the consolidated material to have a laminar microstructure, with $Bi_2Te_{3-x}Se_x$ layers extending several microns in the cylinder plane and with thicknesses of *ca.* 50 nm (Figure 3). Top-view SEM micrographs from the pressing direction, showed the grains to partially preserve the precursor disk-like geometry, but to have grown considerably in the lateral direction during the hot-pressing.

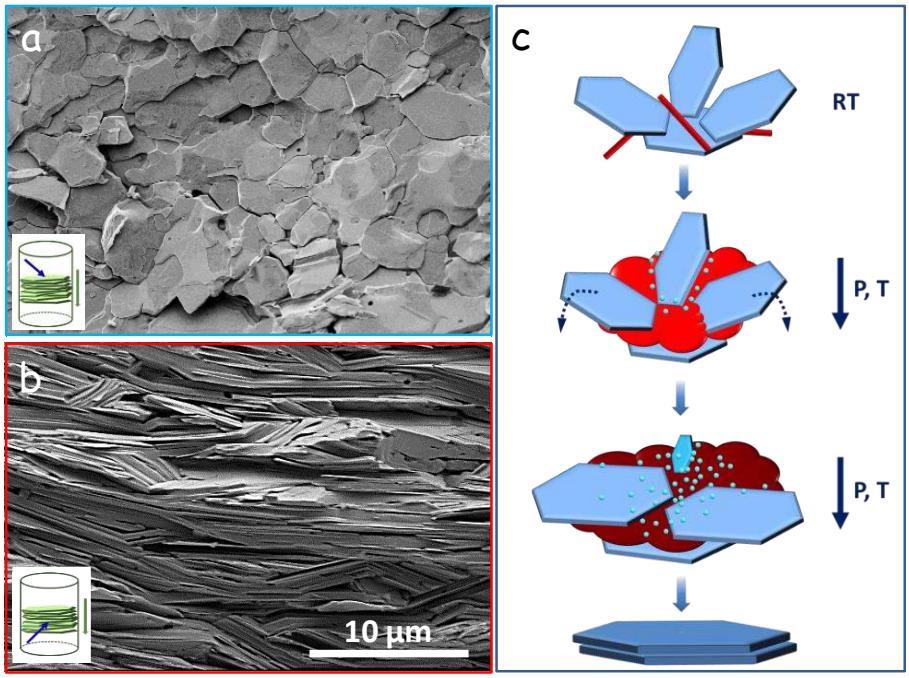

Figure 3. Top-view (a) and cross-section (b) SEM micrographs of a $Bi_2Te_{2.7}Se_{0.3}$ pellet. (c) Cartoon of the mechanism of formation of the crystallographically textured polycrystalline material from the hot pressing of $Bi_2Te_{3-x}Se_x$ nanodisks under an excess of Te (thin red cylinders: Te nanorods; blue disks: $Bi_2Te_{3-x}Se_x$ nanodisks; small blue spheres: Bi, Te and Se atoms; red cloud: liquid Te; garnet cloud: liquid Te containing dissolved Bi and Se atoms). The rotation of the disks aligned close to normal to the pressure axis and the dissolution and reprecipitation within the liquid Te of the disks aligned close to the pressing direction is represented.

The presence of an excess of Te during the hot press step, which was in liquid state, was essential to produce highly textured nanomaterials (Figure S13).

Under a uniaxial pressure, the minimization of both the system entropy and the energy related to the stress accommodation drives the crystals to rotate to have the *c* direction, the one with the lowest elastic modulus, along the pressure axis. Liquid Te aided this rotation by playing a lubricant role.

Besides NC rotation, another mechanism of crystallographic alignment is the NCs dissolution and their recrystallization with the proper crystallographic orientation. Indeed, Bi has a relatively high solubility within liquid Te at the hot pressing temperature (480 ºC), which enabled the NC dissolution and reprecipitation mechanism.[45] Dissolution takes place preferentially at the highest energy facets, *i.e.* those normal to the *ab* plane, and is aided in the pressing direction by the created

stress.[46, 47] Even without stress, $Bi_2Te_{3-x}Se_x$ crystals naturally grow forming plates that extend along the *ab* crystal plane. The presence of a uniaxial pressure favors growth in the direction normal to the pressure axis. At the same time, to minimize energy under the uniaxial pressure, reprecipitating crystals align with their minimum elastic modulus, *i.e.* the *c* direction, along the direction of the stress. Thus, thin and large plates with the *c* direction along the pressure axis were produced.

Overall, both mechanisms might have taken place simultaneously. Disk-shaped NCs initially lying close to normal to the pressure axis might slightly rotate and grow in the *ab* directions from ions coming, through the liquid tellurium, from the dissolution of NCs lying mostly parallel to the pressure axis (Figure 3c).

While the presence of liquid Te was essential to produce highly textured nanomaterials, close to stoichiometric cation:anion ratios are required to achieve optimum TE properties. Therefore, the removal of the relatively large excess of Te used during the consolidation process was critical. Conveniently, during the hot-press process, the excess amount of Te was expelled through the die-plunger interface, as observed by careful analysis of the plunger insertion region of the die (Figure S14). Nevertheless, the complete removal of Te required cycling up and down the pressure several times during the 210 s that the material was at 480 °C (Table 1). This pressure cycling also aided texturization, *i.e.* an improved crystal texture was obtained in pellets produced with a cycled pressure as compared to those hot-pressed at constant pressure. We hypothesize that the compression and decompression of the pellet during each cycle, extending *ca.* 1 μm, could aid rotation and reorientation of the NCs. Additionally, the texture improvement with cycling might in part be associated with the more efficient removal of the Te excess. When cooling down, all the liquid material randomly crystallizes, reducing texture. Thus, an efficient removal of Te during consolidation resulted in no material randomly crystallizing when cooling down at the end of the hot pressing process.

Within its experimental error, EDX analysis of the consolidated materials showed them to have close to stoichiometric cation:anion ratios (Table 1) with Te:Se ratios closely following the nominal compositions (once removed the Te excess). However, extensive STEM-EELS analysis of a thinned cross section of the pellet demonstrated the presence of abnormally large amounts of Te at a significant number of crystal interfaces (Figures 4b and S15).

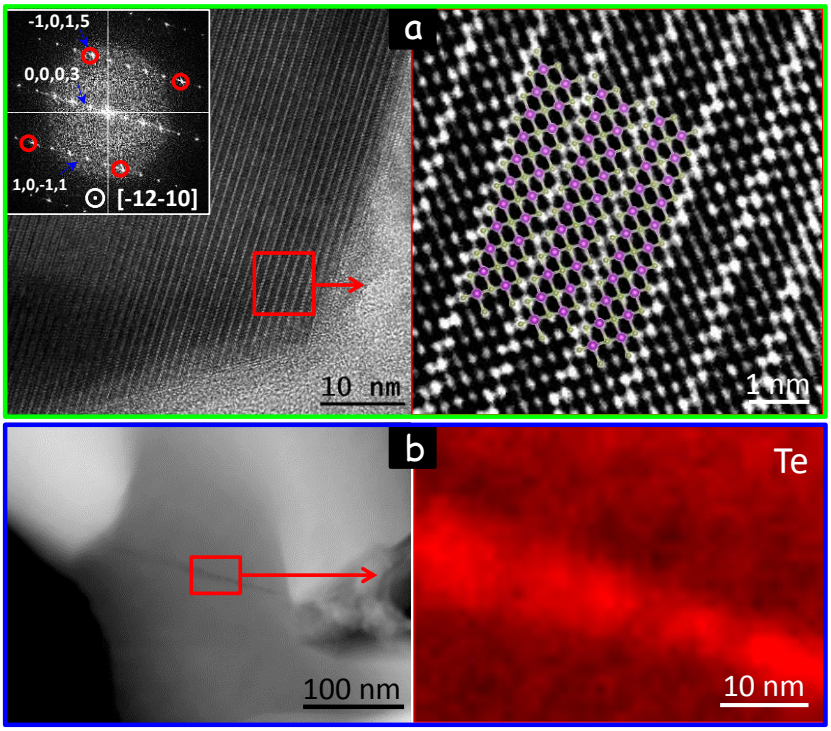

Figure 4. (a) HRTEM image of a $Bi_2Te_{2.7}Se_{0.3}$ crystal within a consolidated pellet. The corresponding power spectrum, consistent with the [-12-10] zone axis of the $Bi_2Te_{2.7}Se_{0.3}$ structure, is shown as an inset. Also shown (right) a detail of the squared region of the HRTEM image overlaid with the structure of $Bi_2Te_{2.7}Se_{0.3}$: Bi in purple, Se and Te in green, with partial occupations on the same sites. (b) ADF-STEM (left) and STEM-EELS Te composition map (right) of the interface of two crystals within the consolidated pellet, showing an excess of Te.

Thermoelectric characterization

From the consolidated cylinders, rectangular bars were cut in two directions, along the press axis, *i.e.* the cylinder length, and within the plane normal to this axis, *i.e.* the cylinder disk plane (Figure 5).

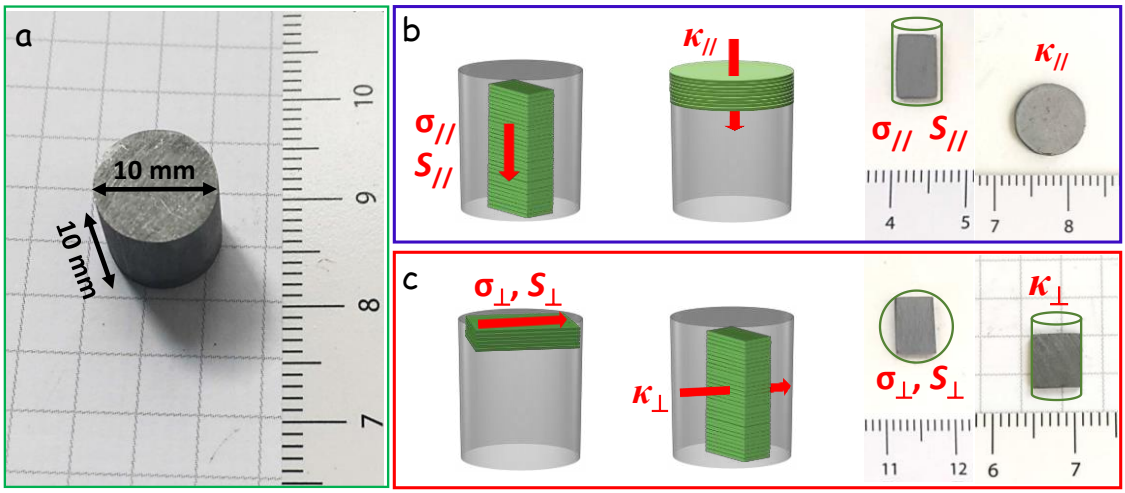

Figure 5. (a) Photograph of a cylindrical pellet produced by hot pressing. b-c) Schematic illustrations and photographs of the samples obtained from the cylindrical pellets and used to measure TE properties in each direction, parallel (b) and normal (c) to the pressure axis. Electrical conductivities (σ) and Seebeck coefficients (S) were always measured using rectangular samples. Thermal conductivities (κ) were measured from disk-shaped samples in the direction of the pressing direction and from rectangular samples in the direction normal to the pressing direction. Rectangular and disk-shaped samples were represented as a pile of layers to schematize the preferential crystallographic orientation within the samples.

Figures 6 and 7 display the electrical conductivity (σ), Seebeck coefficient (S), power factor (PF), total thermal conductivity (κ), the total thermal conductivity once subtracted the electronic contribution ($\kappa - \kappa_e$), and the TE figure of merit (ZT) of the $Bi_2Te_{3-x}Se_x$ (x = 0, 0.2, 0.3, 0.4, 0.5 and 0.7) pellets measured in the two directions, parallel (//) and perpendicular ($\perp$) to the pressure axis. Figure 8 displays the dependence of the same parameters on the Se concentration, x. Additionally, Figure 9 displays the comparison between the TE properties of the best performing nanomaterial, $Bi_2Te_{2.7}Se_{0.3}$, and a commercial ingot measured in two normal directions, the cleavage plane, *i.e.* the *ab* plane, and its normal, *i.e. c* direction (Figure S16).

All $Bi_2Te_{3-x}Se_x$ pellets displayed a degenerated semiconductor behavior, with σ monotonically decreasing with temperature in all the temperature range measured (Figures 6a and 6b). σ decreased with the amount of Se (x, Figure 8a). Generally, Te-rich Bi_2Te_3 has an *n*-type character because σ is dominated by positively charged antisite defects, Te_{Bi}.[48] Such defects are abundant due to the similar ionic radius and electronegativity of Te and Bi, providing charge carrier concentrations in the range 10^{18}-10^{20} cm^{-3}.[48] The decrease of the σ of $Bi_2Te_{3-x}Se_x$ pellets with Se

was related to a reduction of the concentration of the dominant *n*-type point defect, Te_{Bi}. This reduction was associated with the smaller radius and higher electronegativity of Se compared with Te and Bi, which made the formation of Se_{Bi} antisites much less energetically favorable than Te_{Bi}. Actually, the dominant point defects in *n*-type Bi_2Se_3 are not Se_{Bi} antisites, but positively charged Se vacancies, which are not favored in an ambient with an excess of chalcogen as the one used to process our nanomaterials.

As expected, all samples exhibited much higher σ in the cylinder plane ($\sigma_{\perp}$) than in the pressing direction ($\sigma_{//}$), *e. g.* $\sigma_{\perp}/\sigma_{//} = 2.3$ for $Bi_2Te_{2.7}Se_{0.3}$ at 320 K, which was related to the higher charge carrier mobility in the *ab* crystal plane than in the *c* direction (Figures 6a and 6b). At first view surprisingly, σ was higher for nanomaterials than commercial samples (Figure 9a). This result was related to the higher charge carrier concentrations obtained in our nanomaterials compared with the commercial ingot. Hall measurements at room temperature showed the charge carrier concentration of $Bi_2Te_{2.7}Se_{0.3}$ nanomaterials, $n_H = 7 \pm 2 \times 10^{19}$ cm^{-3}, to be a 3.5 fold higher than in the commercial sample, $n_H = 2.0 \pm 0.5 \times 10^{19}$ cm^{-3}. These higher charge carrier concentrations were related to the highly Te-rich environment used for their processing, which translated in a larger concentration of Te_{Bi} antisites. Additionally, the elemental Te present at grain boundaries (Figure 4b) could contribute to further increase *n* through spillover of electrons from these Te domains to the $Bi_2Te_{3-x}Se_x$ matrix, owing to the lower work function of the former (Figure 10).[5, 17]

As expected, charge carrier mobilities in the commercial samples were sensibly higher than in the nanomaterial: $\mu_H = 286$ cm^{2}V^{-1}s^{-1} for the commercial sample in the cleavage plane; $\mu_H = 136$ cm^{2}V^{-1}s^{-1} for the nanomaterial in the direction normal to the pressure axis; $\mu_H = 71$ cm^{2}V^{-1}s^{-1} for the commercial sample in a plane normal to the cleavage plane; $\mu_H = 61$ cm^{2}V^{-1}s^{-1} for the nanomaterial in the pressing direction.

Negative *S* values were measured for all samples in the whole temperature range, in agreement with the *n*-type character of the materials (Figures 6c, 6d and 8b). The absolute value of *S* increased gradually up to 450 K and flattened at higher temperatures, with the rise of the bipolar contribution. *S* absolute values increased with the amount of Se, consistently with the decrease of the charge carrier concentration associated to the replacement of Te with Se. *S* values measured in the two directions were very similar, *e.g.* $S_{//}/S_{\perp} = 1.1$ for $Bi_2Te_{2.7}Se_{0.3}$ at 320 K, which was consistent with the low anisotropy of this parameter (Figure 9b).[36] Absolute *S* values of the

nanomaterials were significantly lower than those of commercial ingots, consistently with their higher charge carrier concentrations. These higher charge carrier concentrations also explained the lower absolute *S* decrease due to the bipolar contribution observed in the high temperature region measured for the nanomaterial when compared with the commercial ingot.

For nanomaterials, *PFs* calculated in the pressing direction were lower than those calculated in its normal (Figures 6e, 6f and 8c). In the normal direction, *PFs* up to 2.86 $Wm^{-1}K^{-2}$ at 350 K were reached. The highest *PFs* measured in the pressing direction were obtained for $Bi_2Te_{2.7}Se_{0.3}$ and $Bi_2Te_{2.8}Se_{0.2,}$ and in the cylinder plane for Bi_2Te_3, $Bi_2Te_{2.8}Se_{0.2}$ and $Bi_2Te_{2.7}Se_{0.3}$. Compared with commercial ingots (Figure 9c), *PFs* of nanomaterials were lower than those measured in the cleavage plane of commercial ingots, due to the higher *S* of the later, but higher than in the direction normal to the cleavage plane, due to the low σ of the commercial sample in this direction.

As expected from the microstructure of the nanomaterial pellets, κ in the pressing direction was much lower than in the cylinder plane for all samples, *e.g.* $\kappa_{\perp}/\kappa_{/\!/} = 2.5$ for $Bi_2Te_{2.7}Se_{0.3}$ at 320 K (Figure 9d). In the low temperature range, κ decreased with temperature to later slightly rise with the emergence of the bipolar contribution. This bipolar contribution strongly decreased with the amount of Se introduced due to the band gap increase, as observed in Figures 7c and 7d. κ also decreased with Se due to the higher lattice disorder (Figure 8d).

After having subtracted the electronic contribution κ_e, κ decreased with temperature in the low temperature range and stabilized or increased at higher temperatures, when the bipolar contribution, κ_{bi}, became significant (Figure 9e). Above the Debye temperature, *ca.* 145 K for Bi_2Te_3,[49] phonon scattering by Umklapp mechanism leads to a T^{-1} dependence of the lattice thermal conductivity, κ_L. On the other hand, κ_{bi} displays an exponential dependence with temperature and the material band gap, E_g:[50]

$$\kappa_{bi} \propto exp(-\frac{E_g}{2\kappa_B T}) \quad (1)$$

To estimate κ_{bi}, we linearly fitted (κ-κ_e) vs. T^{-1} in the low temperature range and extrapolated data to higher temperatures (Figure S17).

At room temperature, compared with commercial ingots, with κ_L ~ 1.1 $Wm^{-1}K^{-1}$ along the cleavage plane and κ_L ~ 0.43 $Wm^{-1}K^{-1}$ normal to this plane (Figure 9e), nanocrystalline $Bi_2Te_{3-x}Se_x$ samples displayed significantly lower κ_L, even when correcting for the smaller relative densities, *ca.* 93 %. Taking into account the porosity correction, *i.e. ca.* 20% modification, $Bi_2Te_{3-x}Se_x$ samples displayed κ_L ~ 0.74 $Wm^{-1}K^{-1}$ in the cylinder plane and κ_L ~ 0.25 $Wm^{-1}K^{-1}$ in its normal

direction. These low κ_L were associated to the large density of grain boundaries, interphase Te and crystal defects such as stacking faults. Notice that the κ_L values obtained were still above the theoretical minimum calculated using the half-wavelength model proposed by Cahill $\kappa_{Lmin} = 0.14$ - 0.18 $Wm^{-1}K^{-1}$,[51] and values reported for $Bi_2Te_{2.7}S_{0.3}/Bi_2Te_3$ hetero-nanosheets (0.2 $Wm^{-1}K^{-1}$ at 300 K),[52] highly defective Bi_2Te_3 (*ca.* 0.17 $Wm^{-1}K^{-1}$),[53] small Bi_2Te_3 nanograins (0.12 $Wm^{-1}K^{-1}$) and stacked Bi_2Te_3 2D films (0.1 $Wm^{-1}K^{-1}$).[54]

In $Bi_2Te_{3-x}Se_x$ nanomaterials the κ_{bi} contribution was substantially lower than in commercial ingots and started to be appreciated at higher temperatures, ~ 400 K (Figures 9e and S17). This reduced κ_{bi} contribution in $Bi_2Te_{3-x}Se_x$ nanomaterials, was mainly attributed to the larger density of majority charge carriers of the former.[55, 56] Additionally, the selective scattering of minority carriers at the intergrain energy barriers introduced by the elemental Te (Figure 10) could also contribute to the reduction of the bipolar contributions and particularly κ_{bi} in $Bi_2Te_{3-x}Se_x$ nanomaterials.[18, 57]

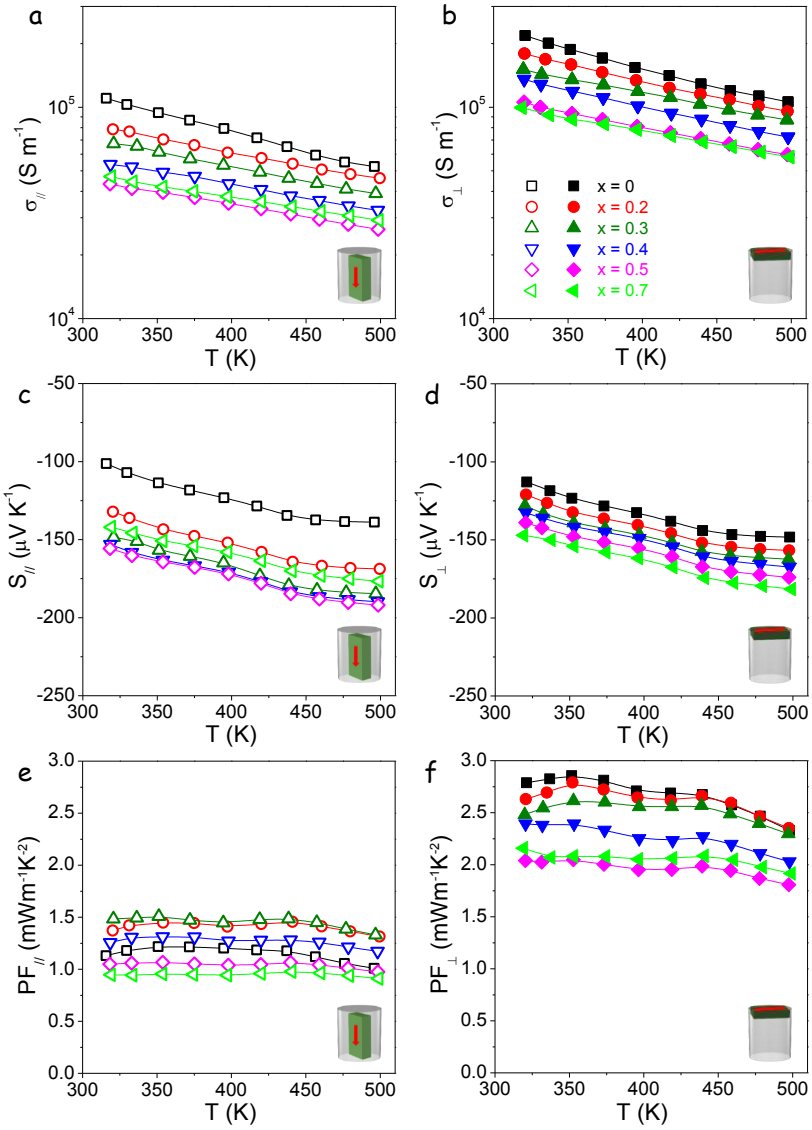

Figure 6. Thermoelectric properties of $Bi_2Te_{3-x}Se_x$ (x = 0, 0.2, 0.3, 0.4, 0.5 and 0.7) nanomaterials measured in the pressing direction (//, left column, open symbols) and in the plane normal to the pressing direction (⊥, right column, solid symbols): (a,b) electrical conductivities, $\sigma_{//}$, $\sigma_{\perp}$; (c,d) Seebeck coefficients, $S_{//}$, $S_{\perp}$; (e,d) power factors, $PF_{//}$, $PF_{\perp}$.

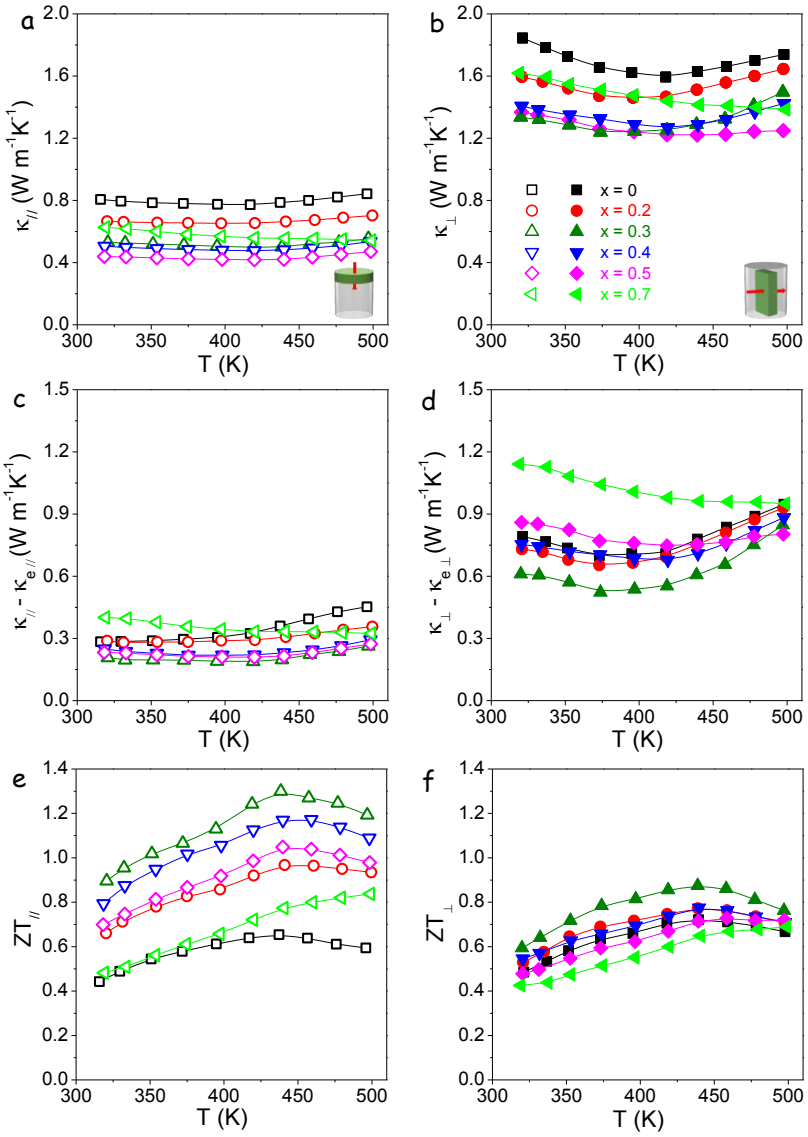

Figure 7. Thermoelectric properties of $Bi_2Te_{3-x}Se_x$ (x = 0, 0.2, 0.3, 0.4, 0.5 and 0.7) nanomaterials measured in the pressing direction (//, left column, open symbols) and in the plane normal to the pressing direction (⊥, right column, solid symbols): (a,b) total thermal conductivity, $\kappa_{//}$, $\kappa_{\perp}$; (c,d) thermal conductivity after subtraction of electronic component, $\kappa_{//} - \kappa_{e//}$, $\kappa_{\perp} - \kappa_{e\perp}$; (e,f) TE figures of merit, $ZT_{//}$, $ZT_{\perp}$.

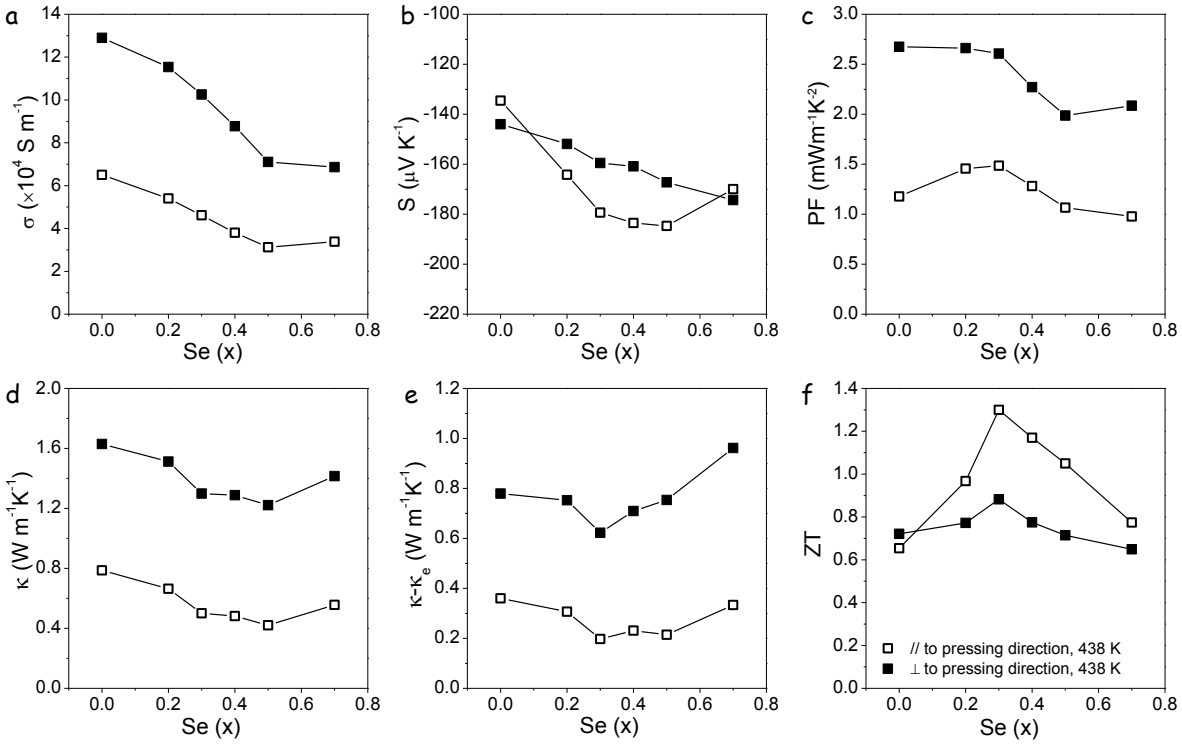

Figure 8. Dependence with the Se concentration (x) of the electrical conductivity, σ (a); Seebeck coefficient, S (b); power factor PF (c); total thermal conductivity κ (d); thermal conductivity after subtraction of electronic component, κ-κ_e (e), and TE figure of merit ZT (f), of $Bi_2Te_{3-x}Se_x$ pellets measured in the two directions, parallel (//) (open symbols, □) and normal (⊥) (solid symbols, ■) to the pressing direction at 438 K.

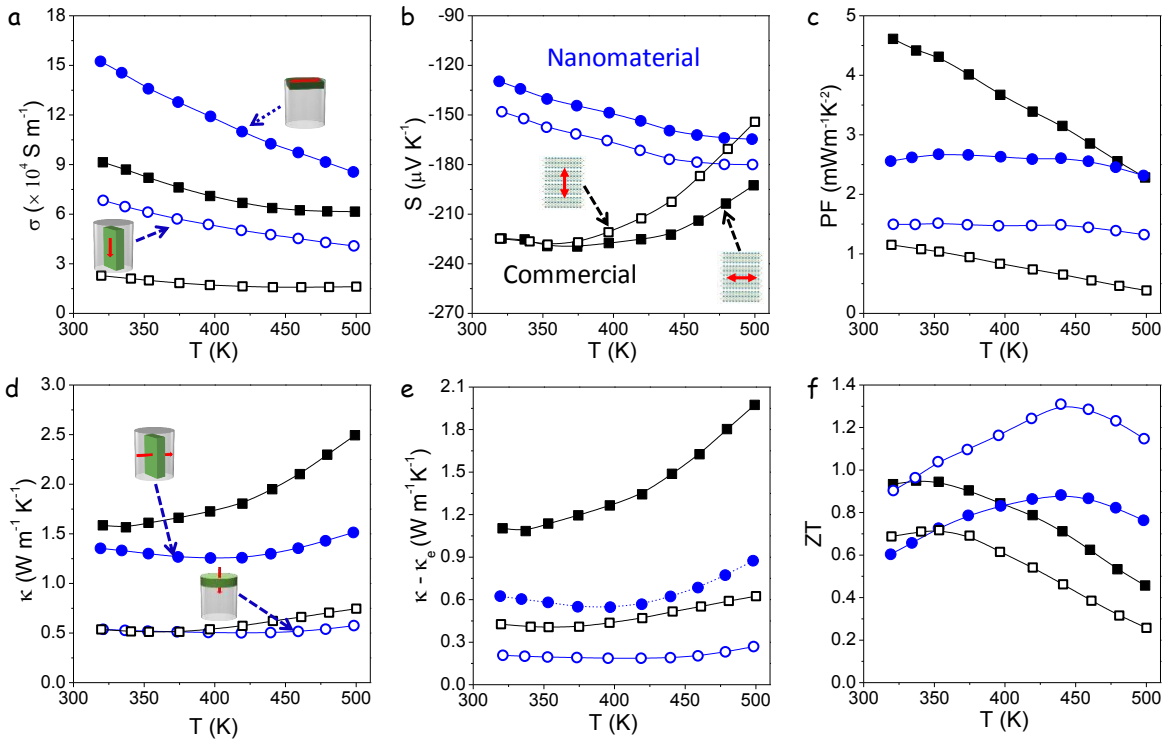

Figure 9. TE properties of $Bi_2Te_{2.7}Se_{0.3}$ nanomaterials measured in two directions, parallel (open blue circles, ○) and normal (solid blue circles, ●) to the pressing direction; and a commercial ingot measured in two directions, parallel (open black squares, □) and normal (solid black squares, ■) to the *c* crystallographic direction: (a) σ; (b) *S*; (c) *PF*; (d) κ; (e) κ-κ_e; and (f) *ZT*. Nanomaterial data was obtained from averaging the experimental results from 5 samples with the same composition.

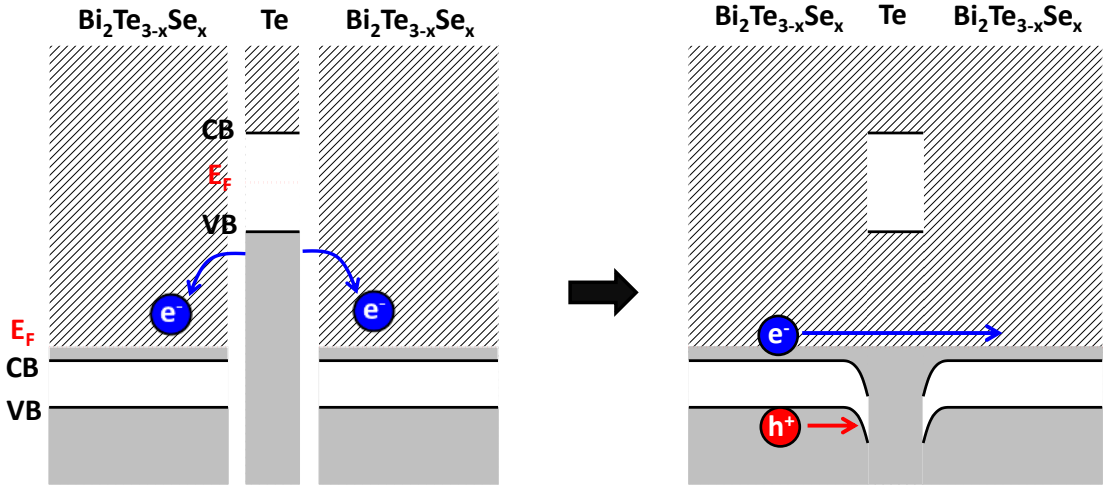

Figure 10. Scheme of the energy band alignment between Te (Φ = 4.7 eV; *Eg* = 0.33-0.36 eV)[58-60] and $Bi_2Te_{3-x}Se_x$ (Bi_2Te_3: Φ = 5.30 eV; *Eg* = 0.17 eV),[61, 62] underlying the charge injection from Te to $Bi_2Te_{3-x}Se_x$

and the barrier for hole transport that Te introduce within $Bi_2Te_{3-x,}Se_x$.

Overall, among the different compositions tested, $Bi_2Te_{2.7}Se_{0.3}$ displayed the highest *ZT* values (Figures 7e, 7f and 9f). *ZT* values in the pressing direction, *i.e.* the direction of preferential *c* crystallographic orientation, were systematically higher than in its normal directions, the *ab* plane, due to the predominance of κ suppression in *c* over σ gain in *ab* (Figures 7a and 7b). Averaging the data measured from 5 pellets with very similar composition, $Bi_2Te_{2.7}Se_{0.3}$, the highest *ZT* value, $ZT = 1.31$, was reached at 438 K in the pressing direction (Figures S18 and S19). Even more important, due to the lower bipolar contributions, very high *ZT* values were sustained in an extended temperature range. The average *ZT* for nanocrystalline $Bi_2Te_{2.7}Se_{0.3}$ in the pressing direction, calculated over 180 K, from 320 K to 500 K, was $ZT_{ave} = 1.15$ (Figure S19b), which represents a *ca.* 50 % increase over the best average value calculated for the commercial ingot, $ZT_{ave} = 0.77$. Additionally, nanocrystalline $Bi_2Te_{3-x}Se_x$ also showed good stability when maintained at relatively high temperature, 420 K, for long periods of time (> 60 h, Figure S20) or when cycling it between the room temperate and 500 K (Figure S21).

CONCLUSIONS

In this work, *n*-type $Bi_2Te_{3-x}Se_x$ NCs with disk-like asymmetric shapes and tuned composition (x = 0, 0.2, 0.3, 0.4, 0.5 and 0.7) were produced in solution. Excess amounts of Te were incorporated in the form of Te nanorods at the NC synthesis step. Such NCs were used to produce high density $Bi_2Te_{3-x}Se_x$ bulk nanomaterials with marked crystallographic texture through hot-pressing them at a temperature above Te melting point. The TE properties of NC-based bulk nanomaterials were measured in two perpendicular directions, along the pressure axis, *i.e.* the direction of preferential *c* crystallographic orientation, and normal to it, with preferential *ab* crystal plane. Nanomaterials were characterized by higher electrical conductivities but lower Seebeck coefficients than commercial materials, which was associated to the higher charge carrier concentrations of the former due to their processing in an excess of Te. Nanomaterials also showed notably lower bipolar contributions, which was in most part also related to the higher charge carrier concentrations, but which could be also influenced by a preferential scattering of minority charge carriers at Te-rich grain boundaries. Record TE figures of merit, $ZT \sim 1.31$ at 438 K were measured from the $Bi_2Te_{2.7}Se_{0.3}$ nanomaterial in the pressing direction. In addition, the high *ZT* values extended over a larger temperature range, from 320 K to 500 K, resulting in *ZT* average values as high as $ZT_{ave} = 1.15$.

EXPERIMENTAL

Chemicals and solvents: Bismuth (III) nitrate pentahydrate ($Bi(NO_3)_3 \cdot 5H_2O$, ≥ 99.99%), sodium selenite (Na_2SeO_3, ≥ 98%), potassium hydroxide (KOH, ≥ 98%), and polyvinylpyrrolidone (PVP, $(C_6H_9NO)_n$, average mol *wt* ~55,000) were purchased from Sigma Aldrich. Sodium tellurite (Na_2TeO_3, 99.5%) and ethylene glycol (EG, $HOCH_2CH_2OH$, 99%) were purchased from Fisher. Analytical grade acetone and ethanol were obtained from various sources. All chemicals were used as received without further purification. Syntheses were carried out using a standard vacuum/dry argon Schlenk line.

Synthesis of $Bi_2Te_{3-x}Se_x$ NCs with Te excess: $Bi_2Te_{3-x}Se_x$ NCs with Te excess were synthesized following a modified polyol process using EG as a high boiling point solvent and reducing agent.[23, 31-33, 42-44] In a typical synthesis of 5 mmol of $Bi_2Te_{3-x}Se_x$ (x = 0, 0.2, 0.3, 0.4, 0.5 and 0.7) NCs with a 25 mol% excess of Te, 10 mmol $Bi(NO_3)_3 \cdot 5H_2O$, 5x mmol of Na_2SeO_3, [5×(3-x)×(1+0.25)]

mmol of Na_2TeO_3, 50 mmol of KOH and 0.5 g of PVP were dissolved in 200 ml of EG within a 500 ml three-neck flask by stirring under argon atmosphere at room temperature for 20 min. Then the solution was heated to 185 ºC. During this process, above 150 ºC, the color of the solution gradually changed from slightly brown to black. Finally, the reaction mixture was kept at 185 °C for 3 h. After this time, the solution was naturally cooled to room temperature by removing the heating mantle. NCs were purified in a multi-step process using various solvents to remove the different impurities. Notice that a proper NC purification was essential to produce nanomaterials with optimized TE properties. In a first step, the solid product was collected by adding acetone to the solution and centrifuging it. In a second step, ethanol was used to redisperse the NCs and acetone ($V_{ethanol}/V_{acetone}$ = 1:2) to precipitate them again. In a third step, deionized water was added to solubilize remaining impurities and NCs were precipitated by slow centrifugation. This 3rd step was repeated twice. In a last step, NCs were redispersed with ethanol and precipitated with acetone, like in step two. Finally, NCs were dried under vacuum at room temperature. This synthesis protocol was optimized to produce almost 4 g of NCs per batch, which was the amount required for a complete characterization of their TE properties at the laboratory scale.

Bulk nanomaterial consolidation: Dried $Bi_2Te_{3-x}Se_x$ (x = 0, 0.2, 0.3, 0.4, 0.5 and 0.7) NCs were annealed at 350 °C for 60 min under an Ar flow inside a tube furnace. The annealed NC, in the form of a powder, were loaded into a graphite die and compacted into cylinders (Ø 10 mm×10 mm) using a custom-made hot press. This process was carried out within a glove box having an argon atmosphere. The hot press temperature was set at 480 ºC and pressure was increased up to 70 MPa and released for 5 times during the 210 s that the material was kept at 480 ºC. This pressure cycling was found fundamental to remove the excess of tellurium from the sample and to reach proper crystal texture. When materials with an excess of tellurium were hot pressed in these conditions, the relative densities of the compacted pellets were measured by the Archimedes' method and found to be around 93 % of the theoretical value. From these cylinders, rectangular bars of about 8 × 6 × 1 mm^3 were cut in two normal directions, along the pressing direction and within the cylinder plane. As a reference material, we characterized a commercial *n*-type ingot obtained from Huabei Cooling Device Co., Ltd, China. Within the EDX experimental error (*ca.* 3 %), the composition of the commercial ingot was $Bi_2Te_{2.68}Se_{0.27}$. Using the Archimedes' method, we measured a density of this ingot to be ~7.7 g/cm^3.

Structural and chemical characterization: X-ray diffraction (XRD, 2θ angle: 20° to 80°; scanning

rate: 5 °/min) analyses were carried out on a Bruker AXS D8 ADVANCE X-ray diffractometer with Cu–Kα radiation (λ = 1.5406 Å). Size and morphology of initial NCs were examined by transmission electron microscopy (TEM) using a ZEISS LIBRA 120, operating at 120 kV, and field-emission scanning electron microscopy (SEM) on an Auriga Zeiss operated at 5.0 kV. SEM micrographs were used to obtain an estimate of the NC average size. 100 NCs were measured for this purpose in each sample. Crystallographic structure and chemical composition were analyzed by HRTEM and Electron Energy Loss Spectroscopy (EELS), respectively, using a Tecnai F20 field-emission gun microscope at 200 keV with an embedded Gatan QUANTUM image filter. The material composition was analyzed using an Oxford energy dispersive X-ray spectrometer (EDX) attached to a Zeiss Auriga SEM at 20.0 kV.

Thermoelectric property measurement: Seebeck coefficients were measured by using a static DC method. Electrical resistivity data was obtained by a standard four-probe method. Both the Seebeck coefficient and the electrical resistivity were measured simultaneously in a LSR-3 LINSEIS system in the temperature range between room temperature and 498 K, under helium atmosphere. At each temperature, 3 measurements were taken. Taking into account the system accuracy and the measurement precision, an error of *ca.* 4 % in the measurement of the electrical conductivity and Seebeck coefficient was estimated. The thermal conductivity was calculated by $\kappa = \lambda C_p \rho$, where λ is the thermal diffusivity, C_p is the heat capacity, and ρ is the mass density of the specimen. A XFA 600 Xenon Flash Apparatus was used to determine the thermal diffusivities (λ) of the samples with an estimated error of *ca.* 5 %. The constant pressure heat capacity (C_p) was estimated from empirical formulas by the Dulong–Petit limit (3R law), and the density (ρ) values used here were calculated using the Archimedes' method. To avoid cluttering the plots, error bars were not included in the figures. Hall charge carrier concentrations (n_H) and mobilities (μ_H) at room temperature (300 K) were measured with a Physical Property Measurement System (PPMS-9T, 10 % error, Quantum Design Inc., USA) using a magnetic field of 2 T. Values provided correspond to the average of 5 consecutive measurements.

ASSOCIATED CONTENT

Supporting Information. The Supporting Information is available free of charge on the ACS Publications website. It contains characterization data such as SEM, XRD, additional TE properties and literature comparison.

AUTHOR INFORMATION

Corresponding Authors

* Email: acabot@irec.cat

* Email: dycadavidr@unal.edu.co

ORCID

Yu Liu: 0000-0001-7313-6740

Maria Ibáñez: 0000-0001-5013-2843

Silvia Ortega: 0000-0002-3812-5146

Jordi Arbiol: 0000-0002-0695-1726

Maksym V. Kovalenko: 0000-0002-6396-8938

Doris Cadavid: 0000-0002-1376-6078

Andreu Cabot: 0000-0002-7533-3251

Author Contributions

The manuscript was written through contributions of all authors. All authors have given approval to the final version of the manuscript.

ACKNOWLEDGEMENT

This work was supported by the European Regional Development Funds. YL and YZ thank the China Scholarship Council for scholarship support. M. V. K. acknowledges partial financial support by the European Union (EU) *via* FP7 ERC Starting Grant 2012 (Project NANOSOLID, GA No. 306733). SMS acknowledges funding from "Programa Internacional de Becas "la Caixa"-Severo Ochoa". JD acknowledges funding from the European Union's Horizon 2020 research and

innovation programme under the Marie Sklodowska-Curie grant agreement No. 665919. ICN2 acknowledge funding from Generalitat de Catalunya 2017 SGR 327 and IREC from 2017 SGR 1246 ICN2 members acknowledges support from the Severo Ochoa Programme (MINECO, Grant No. SEV-2013-0295) and is funded by the CERCA Programme / Generalitat de Catalunya. JA, SMS and JD acknowledge funding from MINECO subproject ANAPHASE (ENE2017-85087-C3). Part of the present work has been performed in the framework of Universitat Autònoma de Barcelona Materials Science PhD program.

REFERENCES

1. Bell, L. E. Cooling, Heating, Generating Power, and Recovering Waste Heat with Thermoelectric Systems. *Science* **2008**, *321*, 1457–1461.
2. Snyder, G. J.; Toberer, E. S. Complex Thermoelectric Materials. *Nat. Mater.* **2008**, *7*, 105–114.
3. Kim, S. I.; Lee, K. H.; Mun, H. A.; Kim, H. S.; Hwang, S. W.; Roh, J. W.; Yang, D. J.; Shin, W. H.; Li, X. S.; Lee, Y. H. Dense Dislocation Arrays Embedded in Grain Boundaries for High-Performance Bulk Thermoelectrics. *Science* **2015**, *348*, 109–114.
4. Ortega, S.; Ibáñez, M.; Liu, Y.; Zhang, Y.; Kovalenko, M. V.; Cadavid, D.; Cabot, A. Bottom-Up Engineering of Thermoelectric Nanomaterials and Devices from Solution-Processed Nanoparticle Building Blocks. *Chem. Soc. Rev.* **2017**, *46*, 3510–3528.
5. Ibáñez, M.; Luo, Z.; Genç, A.; Piveteau, L.; Ortega, S.; Cadavid, D.; Dobrozhan, O.; Liu, Y.; Nachtegaal, M.; Zebarjadi, M.; Arbiol, J.; Kovalenko, M.V.; Cabot, A. High-Performance Thermoelectric Nanocomposites from Nanocrystal Building Blocks. *Nat. Commun.* **2016**, *7*, 10766.
6. Mehta, R. J.; Zhang, Y.; Karthik, C.; Singh, B.; Siegel, R. W.; Borca-Tasciuc, T.; Ramanath, G. A New Class of Doped Nanobulk High-Figure-of-Merit Thermoelectrics by Scalable Bottom-Up Assembly. *Nat. Mater.* **2012**, *11*, 233.
7. Yang, L.; Chen, Z. G.; Dargusch, M. S.; Zou, J. High Performance Thermoelectric Materials: Progress and Their Applications. *Adv. Energy Mater.* **2018**, *8*, 1701797.
8. Zhu, T.; Liu, Y.; Fu, C.; Heremans, J. P.; Snyder, J. G.; Zhao, X. Compromise and Synergy in High-Efficiency Thermoelectric Materials. *Adv. Mater.* **2017**, *29*, 1605884.
9. Ding, D.; Lu, C.; Tang, Z. Bottom Up Chalcogenide Thermoelectric Materials from Solution-Processed Nanostructures. *Adv. Mater. Interfaces* **2017**, *4*, 1700517.
10. Zheng, Y.; Luo, Y.; Du, C.; Zhu, B.; Liang, Q.; Hng, H. H.; Hippalgaonkar, K.; Xu, J.; Yan, Q. Designing Hybrid Architectures for Advanced Thermoelectric Materials. *Mater. Chem. Front.*

2017, *1*, 2457–2473.

11. Kim, S.; Yin, F.; Kagawa, Y. Thermoelectricity for Crystallographic Anisotropy Controlled Bi-Te Based Alloys and *p-n* Modules. *J. Alloy. Comp.* **2006**, *419*, 306–311.
12. Kim, S. S.; Aizawa, T. Thermoelectric Properties for *p*-Type $(Bi_2Te_3)_{0.2}(Sb_2Te_3)_{0.8}$ Alloys Fabricated by Shear Extrusion. *Met. Mater. Int.* **2006**, *12*, 317–322.
13. Liu, Y.; Cadavid, D.; Ibánez, M.; De Roo, J.; Ortega, S.; Dobrozhan, O.; Kovalenko, M. V.; Cabot, A. Colloidal $AgSbSe_2$ Nanocrystals: Surface Analysis, Electronic Doping and Processing into Thermoelectric Nanomaterials. *J. Mater. Chem. C* **2016**, *4*, 4756–4762.
14. Liu, Y.; García, G.; Ortega, S.; Cadavid, D.; Palacios, P.; Lu, J.; Ibáñez, M.; Xi, L.; De Roo, J.; López, A. M.; Luo, Z.; Dun, C.; Dobrozhan, O.; Carroll, D.; Zhang, W.; Martins, J.; Kovalenko, M.; Arbiol, J.; Noriega, G.; Song, J.; Wahnon, P.; Cabot, A. Solution-Based Synthesis and Processing of Sn- and Bi-doped Cu_3SbSe_4 Nanocrystals, Nanomaterials and Ring-Shaped Thermoelectric Generators. *J. Mater. Chem. A* **2017**, *5*, 2592–2602.
15. Ibáñez, M.; Korkosz, R. J.; Luo, Z.; Riba, P.; Cadavid, D.; Ortega, S.; Cabot, A.; Kanatzidis, M. G. Electron Doping in Bottom-Up Engineered Thermoelectric Nanomaterials Through HCl–Mediated Ligand Displacement. *J. Am. Chem. Soc.* **2015**, *137*, 4046–4049.
16. Ibáñez, M.; Zamani, R.; Gorsse, S.; Fan, J.; Ortega, S.; Cadavid, D.; Morante, J. R.; Arbiol, J.; Cabot, A. Core-Shell Nanoparticles as Building Blocks for the Bottom-Up Production of Functional Nanocomposites: PbTe-PbS Thermoelectric Properties. *ACS nano* **2013**, *7*, 2573–2586.
17. Liu, Y.; Cadavid, D.; Ibáñez, M.; Ortega, S.; Martí-Sánchez, S.; Dobrozhan, O.; Kovalenko, M. V.; Arbiol, J.; Cabot, A. Thermoelectric Properties of Semiconductor-Metal Composites Produced by Particle Blending. *APL Mater.* **2016**, *4*, 104813.
18. Poudel, B.; Hao, Q.; Ma, Y.; Lan, Y.; Minnich, A.; Yu, B.; Yan, X.; Wang, D.; Muto, A.; Vashaee, D. High-Thermoelectric Performance of Nanostructured Bismuth Antimony Telluride Bulk Alloys. *Science* **2008**, *320*, 634–638.
19. Venkatasubramanian, R.; Siivola, E.; Colpitts, T.; O'quinn, B. Thin–Film Thermoelectric Devices with High Room-Temperature Figures of Merit. *Nature* **2001**, *413*, 597.
20. Goldsmid, H.; Douglas, R. The Use of Semiconductors in Thermoelectric Refrigeration. *Br. J. Appl. Phys.* **1954**, *5,* 386.
21. Kim, Y. M.; Lydia, R.; Kim, J.-H.; Lin, C.-C.; Ahn, K.; Rhyee, J.-S. Enhancement of Thermoelectric Properties in Liquid-Phase Sintered Te-Excess Bismuth Antimony Tellurides Prepared by Hot-Press Sintering. *Acta Mater.* **2017**, *135*, 297–303.
22. Zheng, Y.; Zhang, Q.; Su, X.; Xie, H.; Shu, S.; Chen, T.; Tan, G.; Yan, Y.; Tang, X.; Uher, C. Mechanically Robust BiSbTe Alloys with Superior Thermoelectric Performance: a Case Study of Stable Hierarchical Nanostructured Thermoelectric Materials. *Adv. Energy Mater.* **2015**, *5*,

1401391.

23. Hong, M.; Chen, Z. G.; Yang, L.; Zou, J. $Bi_xSb_{2-x}Te_3$ Nanoplates with Enhanced Thermoelectric Performance due to Sufficiently Decoupled Electronic Transport Properties and Strong Wide-Frequency Phonon Scatterings. *Nano Energy* **2016**, *20*, 144–155.
24. Liu, Y.; Zhang, Y.; Ortega, S.; Ibáñez, M.; Lim, K. H.; Grau Carbonell, A.; Martí-Sànchez, S.; Ng, K. M.; Arbiol, J.; Kovalenko, M. V.; Cadavid, D.; Cabot, A. Crystallographically Textured Nanomaterials Produced from the Liquid Phase Sintering of $Bi_xSb_{2-x}Te_3$ Nanocrystal Building Blocks. *Nano Lett.* **2018**, 18, *4*, 2557–2563.
25. Yu, Y.; He, D.-S.; Zhang, S.; Cojocaru-Mirédin, O.; Schwarz, T.; Stoffers, A.; Wang, X.-Y.; Zheng, S.; Zhu, B.; Scheu, C. Simultaneous Optimization of Electrical and Thermal Transport Properties of $Bi_{0.5}Sb_{1.5}Te_3$ Thermoelectric Alloy by Twin Boundary Engineering. *Nano energy* **2017**, *37*, 203–213.
26. Hu, L.; Wu, H.; Zhu, T.; Fu, C.; He, J.; Ying, P.; Zhao, X. Tuning Multiscale Microstructures to Enhance Thermoelectric Performance of *n*-Type Bismuth-Telluride-Based Solid Solutions. *Adv. Energy Mater.* **2015**, *5*, 1500411.
27. Liu, W. S.; Zhang, Q.; Lan, Y.; Chen, S.; Yan, X.; Zhang, Q.; Wang, H.; Wang, D.; Chen, G.; Ren, Z. Thermoelectric Property Studies on Cu-Doped *n*-Type $Cu_xBi_2Te_{2.7}Se_{0.3}$ Nanocomposites. *Adv. Energy Mater.* **2011**, *1*, 577–587.
28. Yan, X.; Poudel, B.; Ma, Y.; Liu, W.; Joshi, G.; Wang, H.; Lan, Y.; Wang, D.; Chen, G.; Ren, Z. Experimental Studies on Anisotropic Thermoelectric Properties and Structures of *n*-Type $Bi_2Te_{2.7}Se_{0.3}$. *Nano Lett.* **2010**, *10*, 3373-3378.
29. Zhai, R.; Hu, L.; Wu, H.; Xu, Z.; Zhu, T.-J.; Zhao, X.-B. Enhancing Thermoelectric Performance of *n*-Type Hot Deformed Bismuth-Telluride-Based Solid Solutions by Nonstoichiometry-Mediated Intrinsic Point Defects. *ACS Appl. Mater. Interfaces* **2017**, *9*, 28577–28585.
30. Zhu, B.; Huang, Z.-Y.; Wang, X.-Y.; Yu, Y.; Yang, L.; Gao, N.; Chen, Z.-G.; Zu, F.-Q. Attaining Ultrahigh Thermoelectric Performance of Direction-Solidified Bulk *n*-Type $Bi_2Te_{2.4}Se_{0.6}$ *via* Its Liquid State Treatment. *Nano Energy* **2017**, *42*, 8–16.
31. Xu, B.; Feng, T.; Agne, M. T.; Zhou, L.; Ruan, X.; Snyder, G. J.; Wu, Y. Highly Porous Thermoelectric Nanocomposites with Low Thermal Conductivity and High Figure of Merit from Large-Scale Solution-Synthesized $Bi_2Te_{2.5}Se_{0.5}$ Hollow Nanostructures. *Angew. Chem. Int. Ed.* **2017**, *129*, 3600–3605.
32. Park, K.; Ahn, K.; Cha, J.; Lee, S.; Chae, S. I.; Cho, S.-P.; Ryee, S.; Im, J.; Lee, J.; Park, S.-D.; Han, M. J.; Chung, I.; Hyeon, T. Extraordinary Off-Stoichiometric Bismuth Telluride for Enhanced *n*-Type Thermoelectric Power Factor. *J. Am. Chem. Soc.* **2016**, *138*, 14458–14468.
33. Hong, M.; Chasapis, T. C.; Chen, Z.-G.; Yang, L.; Kanatzidis, M. G.; Snyder, G. J.; Zou, J. *n*-Type $Bi_2Te_{3-x}Se_x$ Nanoplates with Enhanced Thermoelectric Efficiency Driven by Wide-

Frequency Phonon Scatterings and Synergistic Carrier Scatterings. *ACS nano* **2016**, *10*, 4719–4727.

34. Prokofieva, L.; Pshenay-Severin, D.; Konstantinov, P.; Shabaldin, A. Optimum Composition of a $Bi_2Te_{3-x}Se_x$ Alloy for the *n*-Type Leg of a Thermoelectric Generator. *Semiconductors* **2009**, *43*, 973–976.
35. Uher, C. *Materials Aspect of Thermoelectricity*. CRC Press: 2016.
36. Carle, M.; Pierrat, P.; Lahalle-Gravier, C.; Scherrer, S.; Scherrer, H. Transport Properties of *n*-Type $Bi_2(Te_{1-x}Sex)_3$ Single Crystal Solid Solutions ($x \leqslant 0.05$). *J. Phys. Chem. Solids* **1995**, *56*, 201–209.
37. Seo, J.; Lee, C.; Park, K. Thermoelectric Properties of *n*-Type SbI_3-doped $Bi_2Te_{2.85}Se_{0.15}$ Compound Fabricated by Hot Pressing and Hot Extrusion. *J. Mater. Sci.* **2000**, *35*, 1549–1554.
38. Srinivasan, R.; McReynolds, K.; Gothard, N. W.; Spowart, J. E. Texture Development During Deformation Processing of the *n*-Type Bismuth Telluride Alloy $Bi_2Se_{0.3}Te_{2.7}$. *Mater. Sci. Eng. A.* **2013**, *588*, 376–387.
39. Zhao, L.; Zhang, B.-P.; Li, J.-F.; Zhang, H.; Liu, W. Enhanced Thermoelectric and Mechanical Properties in Textured *n*-Type Bi_2Te_3 Prepared by Spark Plasma Sintering. *Solid State Sci.* **2008**, *10*, 651–658.
40. Bhame, S. D.; Pravarthana, D.; Prellier, W.; Noudem, J. G. Enhanced Thermoelectric Performance in Spark Plasma Textured Bulk *n*-Type $BiTe_{2.7}Se_{0.3}$ and *p*-Type $Bi_{0.5}Sb_{1.5}Te_3$. *Appl. Phys. Lett.* **2013**, *102*, 211901.
41. Hu, L.; Liu, X.; Xie, H.; Shen, J.; Zhu, T.; Zhao, X. Improving Thermoelectric Properties of *n*-Type Bismuth-Telluride-Based Alloys by Deformation-Induced Lattice Defects and Texture Enhancement. *Acta Mater.* **2012**, *60*, 4431–4437.
42. Yang, L.; Chen, Z.-G.; Hong, M.; Han, G.; Zou, J. Enhanced Thermoelectric Performance of Nanostructured Bi_2Te_3 Through Significant Phonon Scattering. *ACS Appl. Mater. Interfaces* **2015**, *7*, 23694–23699.
43. Anderson, M.; Bharadwaya, S.; Schaak, R. Modified Polyol Synthesis of Bulk-Scale Nanostructured Bismuth Antimony Telluride. *J. Mater. Chem.* **2010**, *20*, 8362–8367.
44. Soni, A.; Yanyuan, Z.; Ligen, Y.; Aik, M. K. K.; Dresselhaus, M. S.; Xiong, Q. Enhanced Thermoelectric Properties of Solution Grown $Bi_2Te_{3-x}Se_x$ Nanoplatelet Composites. *Nano Lett.* **2012**, *12*, 1203–1209.
45. Okamoto, H.; Tanner, L. Bi-Te (Bismuth-Tellurium) Phase Diagram. *ASM* 1986.
46. Kamb, W. B. Theory of Preferred Crystal Orientation Developed by Crystallization under Stress. *J. Geol.* **1959**, *67*, 153–170.
47. Abdullaev, N. Elastic Properties of Layered Crystals. *Phys. Solid State* **2006**, *48*, 663–669.

48. Zhu, T.; Hu, L.; Zhao, X.; He, J. New Insights into Intrinsic Point Defects in V_2VI_3 Thermoelectric Materials. *Adv. Sci.* **2016**, *3*, 1600004.

49. Walker, P. The Thermal Conductivity and Thermoelectric Power of Bismuth Telluride at Low Temperatures. *Proc. Phys. Soc.* **1960**, *76*, 113.

50. Bahk, J.-H.; Shakouri, A. Minority Carrier Blocking to Enhance the Thermoelectric Figure of Merit in Narrow-Band-Gap Semiconductors. *Phys. Rev. B* **2016**, *93*, 165209.

51. Takashiri, M.; Tanaka, S.; Hagino, H.; Miyazaki, K. Combined Effect of Nanoscale Grain Size and Porosity on Lattice Thermal Conductivity of Bismuth-Telluride-Based Bulk Alloys. *J. Appl. Phys.* **2012**, *112*, 084315.

52. Li, S.; Xin, C.; Liu, X.; Feng, Y.; Liu, Y.; Zheng, J.; Liu, F.; Huang, Q.; Qiu, Y.; He, J. 2D Hetero–Nanosheets to Enable Ultralow Thermal Conductivity by All Scale Phonon Scattering for Highly Thermoelectric Performance. *Nano Energy* **2016**, *30*, 780–789.

53. Termentzidis, K.; Pokropyvnyy, O.; Woda, M.; Xiong, S.; Chumakov, Y.; Cortona, P.; Volz, S. Large Thermal Conductivity Decrease in Point Defective Bi_2Te_3 Bulk Materials and Superlattices. *J. Appl. Phys.* **2013**, *113*, 013506.

54. Teweldebrhan, D.; Goyal, V.; Balandin, A. A. Exfoliation and Characterization of Bismuth Telluride Atomic Quintuples and Quasi-Two-Dimensional Crystals. *Nano Lett.* **2010**, *10*, 1209–1218.

55. Liu, W.; Yan, X.; Chen, G.; Ren, Z. Recent Advances in Thermoelectric Nanocomposites. *Nano Energy* **2012**, *1*, 42-56.

56. Hu, L.-P.; Zhu, T.-J.; Wang, Y.-G.; Xie, H.-H.; Xu, Z.-J.; Zhao, X.-B. Shifting Up the Optimum Figure of Merit of *p*-Type Bismuth Telluride-Based Thermoelectric Materials for Power Generation by Suppressing Intrinsic Conduction. *NPG Asia Mater.* **2014**, *6*, e88.

57. Puneet, P.; Podila, R.; Karakaya, M.; Zhu, S.; He, J.; Tritt, T. M.; Dresselhaus, M. S.; Rao, A. M. Preferential Scattering by Interfacial Charged Defects for Enhanced Thermoelectric Performance in Few-Layered *n*-Type Bi_2Te_3. *Sci. Rep.* **2013**, *3*, 3212.

58. Agapito, L. A.; Kioussis, N.; Goddard III, W. A.; Ong, N. Novel Family of Chiral-Based Topological Insulators: Elemental Tellurium under Strain. *Phys. Rev. Lett.* **2013**, *110*, 176401.

59. Kirchhoff, F.; Binggeli, N.; Galli, G.; Massidda, S. Structural and Bonding Properties of Solid Tellurium from First-Principles Calculations. *Phys. Rev. B* **1994**, *50*, 9063.

60. Rigaux, C. Étude de la Structure de Bandes du Tellure par les Phénomènes de Transport. *J. Phys. Chem. Solids* **1962**, *23*, 805–817.

61. Kioupakis, E.; Tiago, M. L.; Louie, S. G. Quasiparticle Electronic Structure of Bismuth Telluride in the GW Approximation. *Phys. Rev. B* **2010**, *82*, 245203.

62. Haneman, D. Photoelectric Emission and Work Functions of InSb, GaAs, Bi_2Te_3 and Germanium. *J. Phys. Chem. Solids* **1959**, *11*, 205–214.

TOC graphical abstract